Focusing a Two-Dimensional Acoustic Vortex Beyond Diffraction Limit on an Ultrathin Structured Surface

Jing-jing Liu, Bin Liang,* and Jian-chun Cheng
Collaborative Innovation Center of Advanced Microstructures and Key Laboratory of Modern Acoustics, MOE, Institute of Acoustics, Department of Physics, Nanjing University, Nanjing 210093, People's Republic of China

(Received 20 August 2020; revised 7 November 2020; accepted 8 December 2020; published 11 January 2021)

We propose and experimentally demonstrate a mechanism for focusing two-dimensional (2D) vortex for airborne sound beyond diffraction limit on an ultrathin structured surface in free space. A simple design of unit cell is presented as a practical implementation, which is capable of exciting evanescent wave and modulating its propagation phase over full 0-to-2π range. By analytically deriving the dispersion relationship and desired azimuthal distribution of effective parameters, we elucidate how to guide the propagation of excited evanescent waves in the vicinity of an unbounded surface decorated with designed structures and focus such surface vortex within a target region despite its compactness and nonaxisymmetry. The effectiveness of our mechanism is demonstrated numerically and experimentally via production and confinement of 2D vortex on a square surface at subwavelength spatial resolution. We anticipate our methodology with no need of a 2D system, bulky device size, geometric symmetry, active elements, or complicated phased array to offer new possibilities for the miniaturization and integration of planar vortex devices and may promote their on-chip applications in various fields such as by significantly boosting the information density and manipulation precision.

DOI: 10.1103/PhysRevApplied.15.014015

I. INTRODUCTION

Vortex beams carrying orbital angular momentum (OAM) have recently attracted rapidly growing interests due to their fundamental significance in wave physics as well as promising potential in diverse applications such as wave-matter interaction [1–6]. A particularly useful example is vortices in two-dimensional (2D) systems where the alternative dimension provided by OAM offers the possibility for manipulating tiny objects and encoding and decoding information, and plays a key role in application of on-chip platforms in various fields ranging from biophysics to acoustofluidics to photonics [7–13]. In comparison to conventional methods relying on numerous active sources that need to be individually addressed to modulate the wave field inside a closed circular region, the recent emergence of artificially engineered structures provides a simple and low-cost solution for the 2D vortex production. But their application potential in practice would have to be hindered by the dependence on an innately 2D system, which needs to be realized by imposing reflective boundary conditions such as with parallel waveguides or liquid-filled microcavities, leading to dramatically increased device size, fabrication difficulty, and mismatch to background medium [14–18].

Furthermore, the spatial resolution of the generated vortex, which is closely related to the information density and manipulation precision, is subject to the diffraction limit. In electromagnetics, plasmonic vortices referring to surface plasmon polaritons (SPPs) have provided an efficient way to generate OAM mode beyond this limit, which can be implemented with the aid of pragmatically designed structures such as Archimedean spirals [19,20] and nanostructures [21,22]. Although the manipulation of acoustic waves at subwavelength scale has been demonstrated to be possible by using gradient-index structures [23–27], twisting of acoustic linear momentum to form an OAM-carrying vortex is difficult to achieve by slowly modulating the spatial distribution of acoustical parameters. Despite the need for the high precision and capacity of various acoustical applications such as particle manipulation and information transfer [28–30], it remains challenging to overcome these limits and produce 2D acoustic vortex with spatial resolution higher than wavelength due to the lack of a direct acoustical analog of SPPs.

In this paper, we propose a mechanism for generating and focusing 2D acoustic vortex for airborne sound beyond the diffraction limit on an unbounded surface decorated with ultrathin structures in free space. As a practical implementation, a simple design of double-layered resonant element (DLRE) with subwavelength physical size is presented, which enables arbitrary and abrupt modulation of transmitted phase of the evanescent wave during its

*liangbin@nju.edu.cn

propagation. By analytically calculating the dispersion relation for the designed unit cell, we derive the desired azimuthal distribution of effective acoustical parameters for producing an evanescent field with a dark spot and phase singularity at its center, representing a strong confinement of OAM information within the target region with nonaxisymmetric geometry and subwavelength spatial resolution. We numerically and experimentally verify the effectiveness of our scheme via several distinctive examples of generating 2D subwavelength acoustic vortices of desired order within a square region as illuminated by simple plane waves.

II. PRODUCTION OF ACOUSTIC EVANESCENT VORTEX

Figure 1 schematically illustrates our proposed mechanism of producing and confining 2D acoustic vortex beyond diffraction limit on an unbounded structured surface by exciting evanescent wave and modulating its propagation phase. As a type of surface acoustic mode carrying OAM, the evanescent vortex in infinite cylindrical coordinate (r, θ, z) can be expressed as

$$p(r,\theta,z) = p_0 J_m(k_{//} r) e^{im\theta} e^{ik_\perp z}, \tag{1}$$

where $k_{//}$ and $k_\perp$ refer to the in-plane and out-of-plane wave-vector components, respectively; p_0 is the pressure amplitude and $J_m(k_{//}r)$ is a mth-order Bessel function of first kind with m being the topological charge. Since such surface vortices should be evanescent along the vertical direction, $k_\perp$ is an imaginary number and thus $k_{//}$ could be much larger than the wave vector k_0 in free space. In order to quantitatively characterize the resolution of the

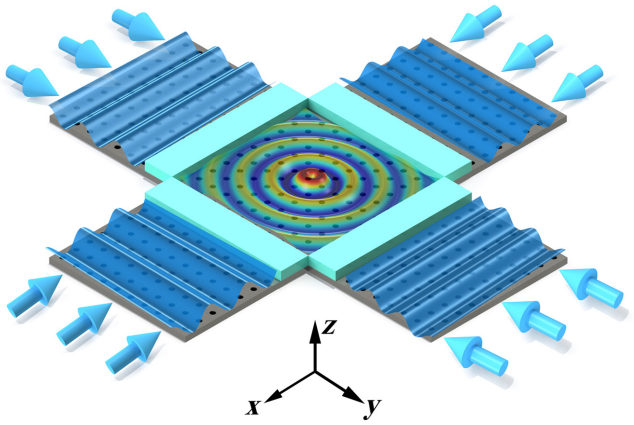

FIG. 1. Schematic of generating and focusing 2D acoustic vortex on an unbounded surface decorated with ultrathin structures whose bottom layer excites and guides the evanescent plane waves along its surface and top layer provides an abrupt phase shift based on our derived formula.

focused dark spot of such evanescent vortices, we introduce a parameter of resolution R, defined as the ratio of mainlobe size of 2D vortex in free space to that of surface vortex, i.e., $R = x_1/x_1'$, where x_1 and x_1' are the first zeros of the mth-order Bessel function in two systems [viz., $J_m(k_0 x_1) = J_m(k_{//} x'_1) = 0$]. Considering $k_0 x_1 = k_{//} x_1'$, R can be expressed as $R = k_{//}/k_0$, which suggests that the resolution depends on the dispersion relationship of the excited acoustic evanescent wave, as discussed later. Benefitting from the near-field and high-spatial-frequency feature of evanescent wave, our mechanism eliminates the dependence on a 2D system and may open up the possibility for generating acoustic evanescent vortex at subwavelength scale. Thus, the excitation and modulation of acoustic evanescent waves play a pivotal role for the realization of such a subwavelength 2D vortex. To date, however, evanescent-wave-based modulations (e.g., subwavelength sound focusing) usually rely on gradient-index structures with bulky size, limited refractive index, and complicated fabrication, which are difficult to find direct application in the generation of surface vortex [23].

III. DESIGN OF DLRE

Here we propose a structure design of DLRE with hitherto inaccessible functionality of guiding evanescent wave effectively while tuning propagation phase abruptly to solve the above difficulties. Then by rationally assembling such building blocks of DLRE to an ultrathin surface with desired acoustical parameters, we implement our mechanism for producing 2D surface vortex, as shown later. We first analyze the dispersion relationship of acoustic evanescent wave guided by the bottom layer of DLRE, i.e., the planar surface periodically decorated with Helmholtz-like subwavelength resonators, as depicted in Fig. 2(a). Solid material for subwavelength resonators is chosen as acrylonitrile-butadiene-styrene (ABS) with density $\rho = 1180$ kg/m^3 and sound speed $c = 2700$ m/s, which can be regarded as acoustically rigid due to the huge contrast between the acoustic impedances of solid and air [31]. The thickness of solid and the lattice constant are $t = 1$ and $a = 20$ mm, respectively. The height and opening width of resonator are $h = 7.5$ and $w = 7$ mm, respectively. Then the pressure and normal velocity of acoustic surface wave propagating on the structured surface are written as

$$\begin{aligned} p &= p_0 e^{-|k_\perp| z} e^{i(k_x x - \omega t)}, \\ v_n &= -\frac{1}{i\omega\rho_a}\frac{\partial p}{\partial z} = -\frac{i|k_\perp|}{\omega\rho_a} p_0 e^{-|k_\perp| z} e^{i(k_x x - \omega t)}, \end{aligned} \tag{2}$$

where ρ_a is the air density, t is time, k_x is the wave vector in the x direction, and ω is the angular frequency. Thus the acoustic impedance at surface $z = 0$, defined as Z_s, can be

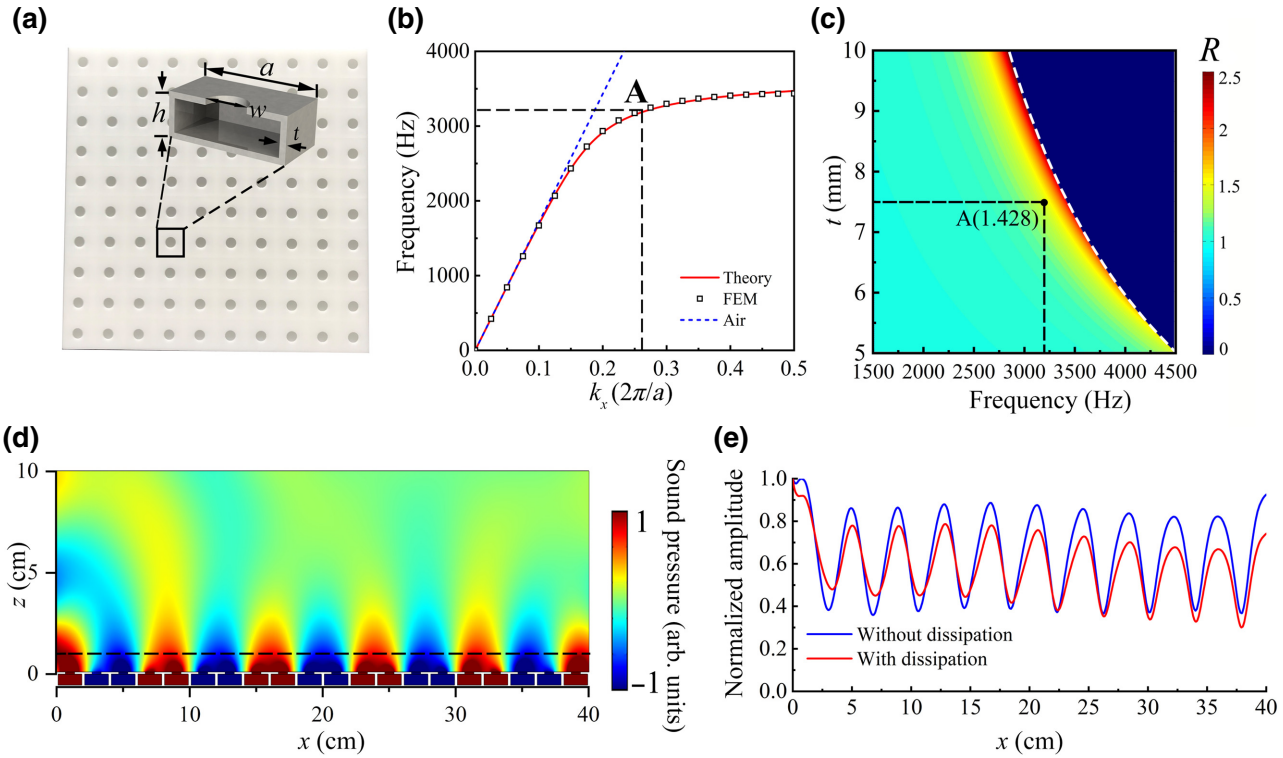

FIG. 2. (a) Prototype of a planar surface periodically decorated with Helmholtz-like subwavelength resonators (photo). Inset: the section view of unit cell. (b) Theoretical and simulated dispersion curve of acoustic evanescent wave with the air dispersion line (denoted by the blue dashed line). (c) The resolution R predicted by Eq. (6) versus frequency and structural parameter t. The white dashed line represents the cut-off frequency of evanescent wave mode. (d) Field distribution of evanescent wave in the x-z plane for a frequency of 3200 Hz. (e) Normalized amplitude profiles along x direction [black dashed line in (d)] in the cases with and without dissipation.

expressed as

$$Z_s = \left.\frac{p}{v_n}\right|_{z=0} = \frac{i\omega\rho_a}{|k_\perp|}. \tag{3}$$

From another perspective of structure, due to the subwavelength scale, the effective surface impedance of three-dimensional (3D) resonators with acoustic mass M_{HR} and capacitance C_{HR} can be regarded as lumped parameters and can be expressed as [32,33]

$$Z_s' = i\left(\frac{1}{\omega C_{\mathrm{HR}}} - \omega M_{\mathrm{HR}}\right)a^2. \tag{4}$$

By applying an impedance continuity condition on the structure's top surface, i.e., $Z_s = Z_s'$, we can derive the dispersion relationship of supported evanescent wave mode, as follows:

$$k_x^2 c_a^2 = \omega^2 + \frac{1}{\left(\omega_{\mathrm{HR}}^2 - \omega^2\right)^2}\frac{(\rho_a c_a)^2\omega^4}{M_{\mathrm{HR}}^2 a^4}, \tag{5}$$

where c_a is sound speed of air in free space and ω_{HR} is resonance frequency of the 3D resonators, respectively. We calculate the dispersion curve of the evanescent waves by using Eq. (5) and plot the result in Fig. 2(b) for an intuitive illustration. Band structure of unit cell calculated by the finite-element method (FEM) is also provided for comparison, which agrees well with the theoretical results. Throughout this paper, we use commercial software COMSOL Multiphysics for the calculation of band structure and the following simulations. As observed, when frequency increases, the dispersion curve starts to deviate from the background line (blue dashed line) and tends to be flat near the edge of the first Brillouin zone, which indicates the excitation of large k_x and corresponding imaginary wave number $k_\perp$ in the vertical direction. It is worth mentioning that the angular dependence of wave vector and the effect of thermal and viscous losses become obvious as the frequency approaches the boundary of the Brillouin zone, resulting in the noncircular equifrequency contours and undesired energy dissipation. In our design, therefore, for ensuring isotropy approximation for $k_{//}$ and keeping high efficiency of the system, we choose the working frequency

slightly away from the band edge. In this case, by substituting k_x into R one can also obtain the analytical expression of resolution of supported evanescent vortex

$$R = \sqrt{1 + \frac{1}{\left(\omega_{\mathrm{HR}}^2 - \omega^2\right)^2} \frac{(\rho_a c_a)^2 \omega^2}{M_{\mathrm{HR}}^2 a^4}}. \tag{6}$$

Obviously Eq. (6) enables a fast and precise prediction of the resolution and information density of OAM. Figure 2(c) depicts the typical theoretical results of resolution R versus the structural parameter t and frequency analytically calculated from Eq. (6). Next, we numerically simulate the field distribution above the structure in the x-z plane at a particular frequency point A(0.26, 3200 Hz) in Fig. 2(b). In contrast to conventional surface acoustic waves that propagate under the surface of solid medium, in our mechanism the produced spoof surface wave is propagating on the upper surface of the structure with rapidly decaying in the vertical direction while taking no account of the sound field below the structured surface, as shown in Fig. 2(d). It is noteworthy that at this frequency the thickness of designed 3D resonators is nearly 15 times smaller than the corresponding wavelength, revealing the advantage of our design over traditional corrugated or perforated structures in terms of downscaled device size (by an order of magnitude) [34–36]. We also simulate the one-dimensional normalized amplitude profiles along the x direction [marked by the black dashed line in Fig. 2(d)] for lossless and lossy models and plot the results in Fig. 2(e). The good agreement between the two curves suggests that our compact and ultrathin design can keep a high efficiency without suffering dramatically from the energy dissipation, which occurs commonly in the process of device miniaturization.

Equation (1) suggests that the phase on the incident boundary should depend linearly on the azimuth angle for the purpose of focusing incident acoustic evanescent wave to OAM-carrying vortex beam. However, although the propagation phase and dispersion characteristic can be engineered via a spatial gradient of structural parameters, the bulky size of gradient-index structure and undesired coupled resonance between adjacent units will make it difficult, if not impossible, to realize the required phase profile, as mentioned above.

Hence, in our design of DLRE, the 3D subwavelength resonator array is topped by another component comprising a series of side-loaded acoustic Helmholtz resonators (HRs), which enables modulating the propagation phase arbitrarily while keeping a subwavelength physical dimension and addresses the above challenges. Figures 3(a) and 3(b) show the illustrative diagram and top view of our designed DLRE, respectively. In such a design, the evanescent wave propagating on the surface of the bottom resonator array will interact effectively with side-loaded

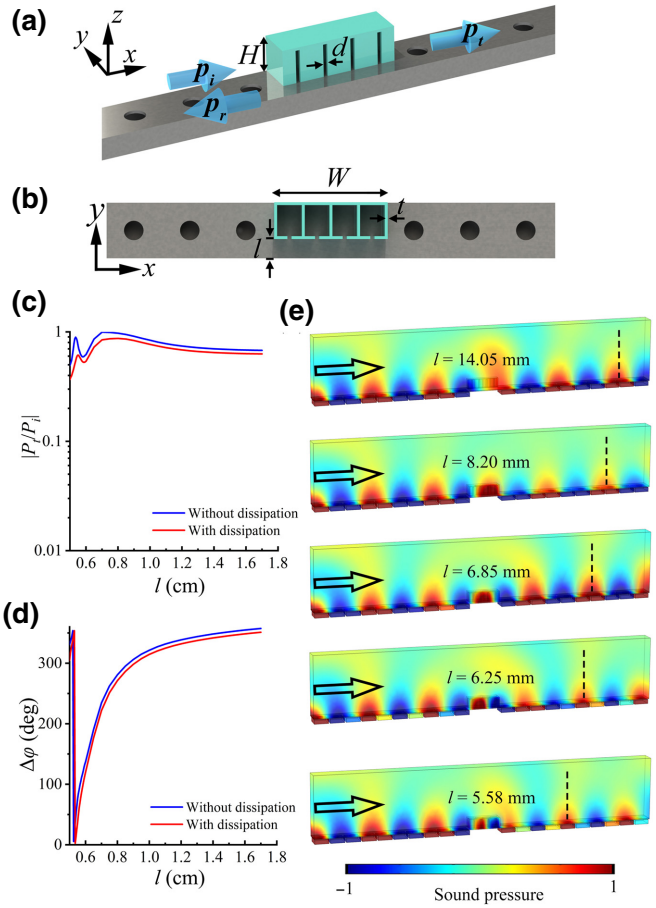

FIG. 3. (a) Illustrative diagram and (b) top view of the proposed DLRE. The structural parameters are chosen as $H = 12.5$ mm, $W = 40$ mm, and $d = 1.5$ mm, respectively. (c) Simulated transmission and (d) phase shift provided by an individual unit cell as a function of l with (red lines) and without (blue lines) dissipation. (e) Simulated sound transmission above individual elements for an equally increased phase shift with a step of $2\pi/5$. Black dashed lines and arrows denote the crests of transmitted waves and incident direction of evanescent waves, respectively.

resonators of superstructure since the eigenfrequencies of two such resonators are designed to be identical, which introduces a large yet controllable phase delay to transmitted wave. Although mode transformation from evanescent to propagating may occur due to the fact that the designed side-loaded HRs cover the openings of the bottom resonators, the in-plane component dominates for the wave vector of propagation mode confined inside each unit cell and will not couple to out-of-plane mode after leaving the superstructure thanks to the deep-subwavelength transversal size of unit cell. On the other hand, the impedance mismatch due to the abrupt changes of the acoustic path's cross section can be significantly compensated by the introduced straight constricted pipe in the superstructure. Besides, the height H of superstructure is elaborately

designed to ensure sufficiently strong interaction with incident evanescent wave while avoiding oversize structure. Furthermore, the scheme enables independent design of each DLRE for tailoring its acoustical response, due to the rigid wall of side-loaded resonators that ensures spatial isolation of evanescent wave between adjacent unit cells. We carry out numerical simulations to retrieve the acoustic response of an individual DLRE and plot the typical results of the transmission coefficient and phase shift as a function of single parameter l in Figs. 3(c) and 3(d) with and without dissipation taken into consideration. The results show that such DLRE can freely modulate the propagation phase of evanescent wave within the full 2π range while keeping a high transmission efficiency despite the subwavelength dimension in all directions and the presence of thermoviscous dissipation, as demanded in our mechanism. For clearer illustration we also simulate the 3D acoustic pressure distribution above single DLRE produced by different structural parameter l and plot the typical results in Fig. 3(e), which shows the desired phase shift with the change of l but no appreciable leaking effect. Note that the maximum thickness of the designed DLRE still did not exceed one fifth of the wavelength, which ensures the compactness and ultrathin profile of the resulting device.

IV. NUMERICAL SIMULATIONS

Next we use numerical simulations to verify the effectiveness of our scheme to focus 2D subwavelength acoustic vortex beyond diffraction limit on an unbounded nonaxisymmetrical surface decorated with designed DLREs. For simplicity without loss of generality, here we use 40 DLREs to assemble an ultrathin square surface with side length of 20 cm as depicted in Fig. 4(a). Such an element number could keep relatively high spatial resolution

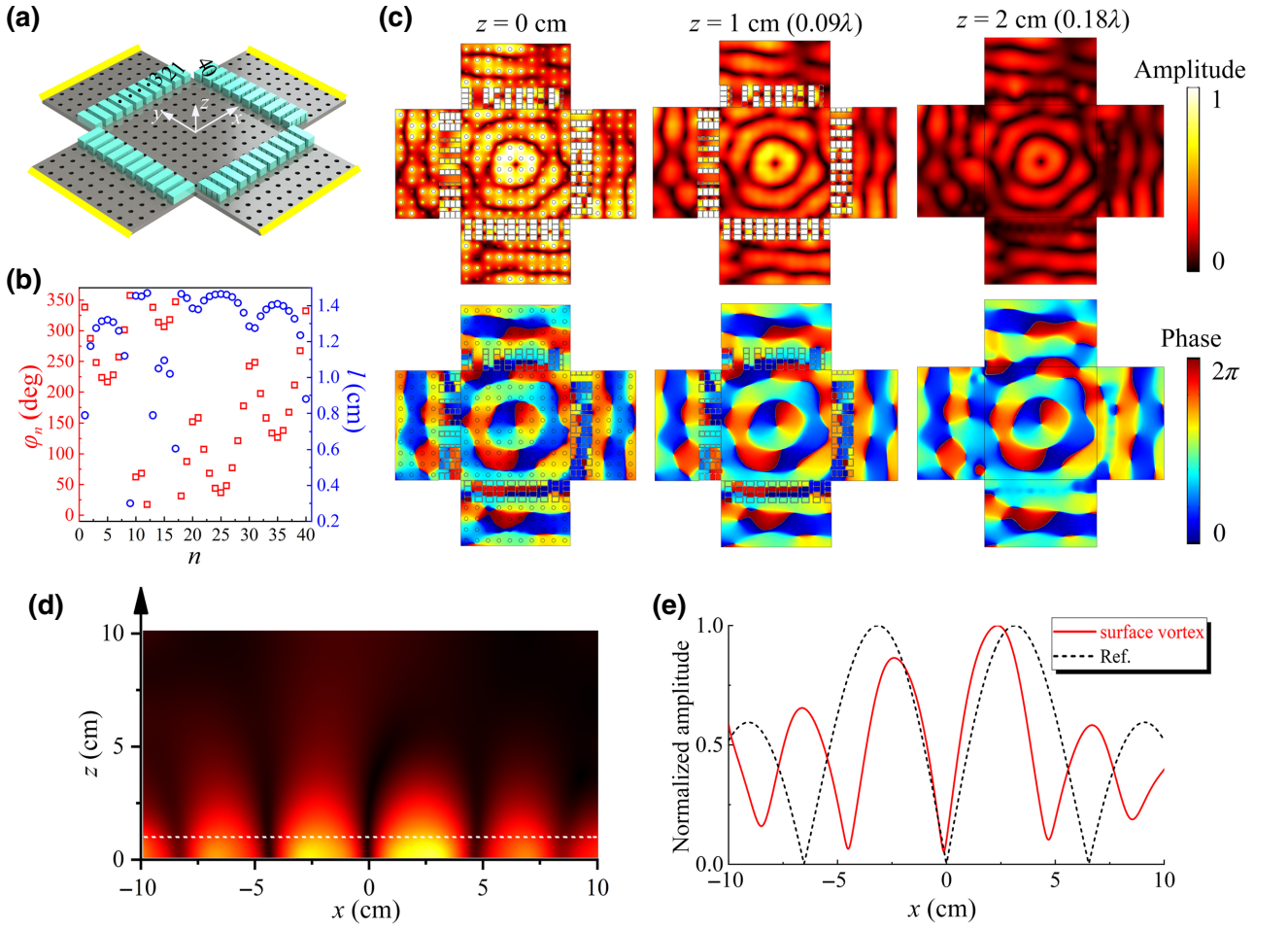

FIG. 4. (a) Schematic illustration of the structured surface consisting of 40 DLREs with a square geometry. Yellow lines denote the line sources. (b) Discrete phase shift predicted by Eq. (7) and corresponding parameter l provided by unit cells for generating first-order 2D vortex. (c) Simulated amplitude and phase distributions in the x-y plane for $z = 0$, 1, and 2 cm. (d) Simulated 2D amplitude distribution in the x-z plane. (e) Normalized pressure amplitude profile along x direction [marked by the dashed line in (d)] in comparison with the theoretical first-order Bessel profile in free space in air.

and eliminate possible spatial aliasing effect while avoiding complicated fabrication. Four identical line sources are placed at the fringes of structured surface [marked by the yellow lines in Fig. 4(a)]. When this device works, the bottom layer excites and guides the evanescent plane wave at subwavelength scale, and the top-layer enclosure provides an abrupt phase shift and modulates this square boundary precisely for twisting incident linear momentum to in-plane OAM. By mapping this physical square boundary to an illusional circle boundary with an additional phase $\Delta\varphi$, we can theoretically derive the ideal continuous phase profile on the square boundary $S(r,\theta)$ for generating mth-order 2D vortex

$$\varphi(r,\theta) = m\theta + \Delta\varphi = m\theta + k_{//}r, \tag{7}$$

where in-plane wave vector $k_{//}$ equals 81 rad/m in our design. For generation of 2D surface vortex with a particular topological charge of $m = 1$, the discrete phase-shift profile theoretically predicted by Eq. (7) and corresponding values of l are illustrated in Fig. 4(b). Figure 4(c)

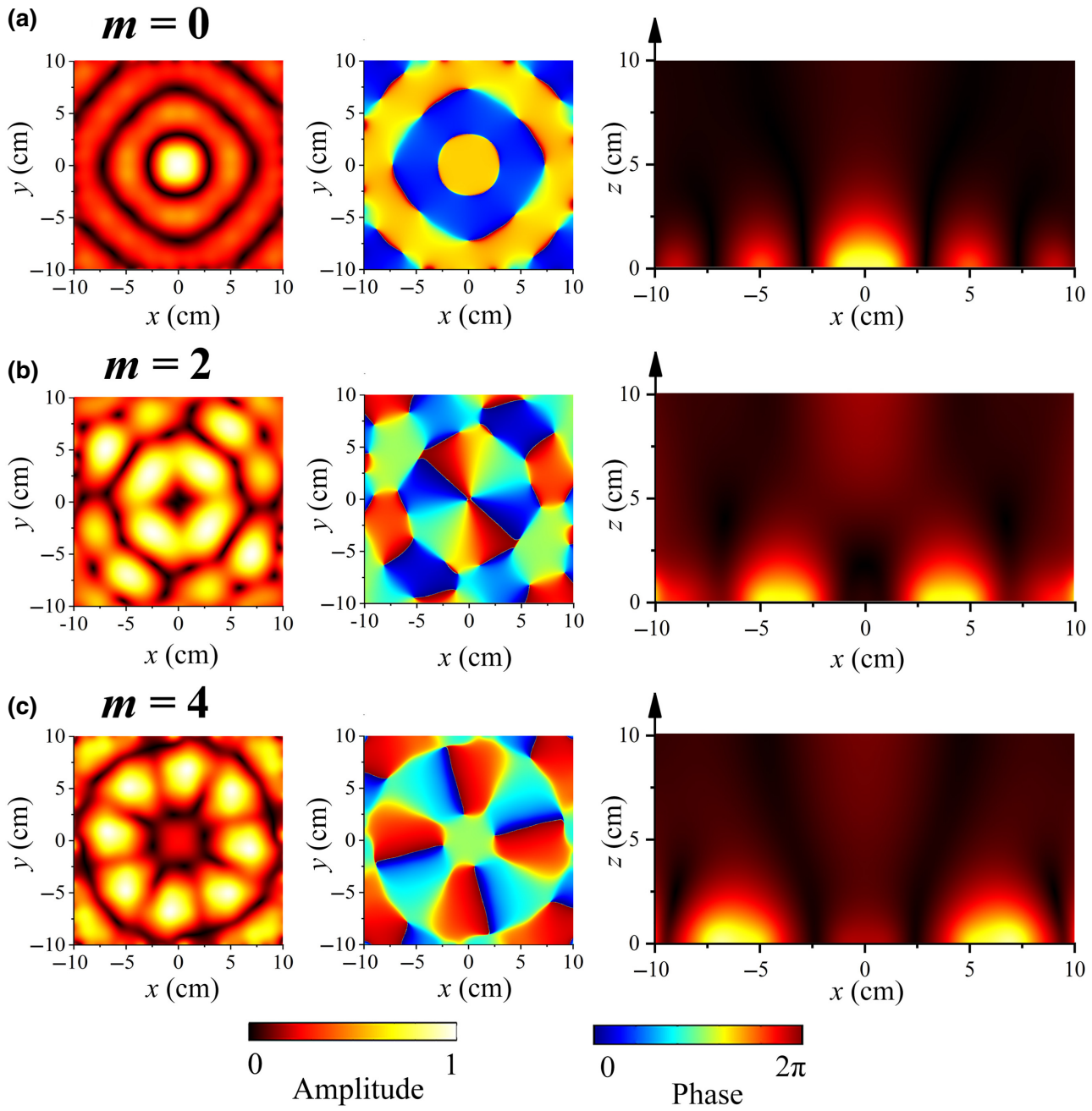

FIG. 5. Simulated normalized amplitude and phase distributions in the x-y plane at $z = 1$ cm and 2D normalized amplitude distribution in the x-z plane with topological charge (a) $m = 0$, (b) 2, and (c) 4.

shows the simulated acoustic pressure amplitude and phase distributions of the produced vortex in the x-y plane for three particular values of $z = 0$, 1, and 2 cm, respectively. We can obviously observe that our scheme gives rise to the first-order vortex beam with typical characteristics of donut-shaped amplitude and spiral phase. Besides effective production of nonaliased vortex beam extending to the whole square enclosure, the relative amplitude of generated vortex decays rapidly away from the structured surface, which indicates the high-efficiency generation and confinement of 2D acoustic vortex with our unbounded ultrathin structured surface. Furthermore, from the phase distributions in three parallel planes in Fig. 4(c) one can also observe the irrotational phase distribution along the z direction, which is a significant feature that differentiates the 2D vortices of our interest from their 3D counterparts propagating in vertical direction. For a clearer illustration we simulate the 2D acoustic pressure distribution in a vertical plane of x-z direction and the corresponding result in Fig. 4(d) shows that most of the energy of this 2D vortex beam is focused and confined in the vicinity of our designed surface, as expected. This breaks through the traditional restriction that the generation of 2D vortices has to rely on a 2D system confined by two indispensable reflective boundaries (e.g., acoustic hard or soft boundary) thanks to the preservation of near-field information carried by the evanescent vortex in unbounded 2D system. Then for exhibiting the subwavelength feature of the surface vortex, we plot the simulated normalized pressure amplitude distribution along the x direction [marked by white dashed line in Fig. 4(d)] and compare it with a theoretical first-order Bessel profile in free space. Figure 4(e) shows that our mechanism produces the desired high-efficiency focus of 2D vortex carrying first-order OAM beyond diffraction limit, as evidence by the remarkably compressed first-order Bessel profile in comparison to that in free space in air. Based on this profile we can numerically calculate the value of the resolution R to be 1.421, which agrees quite well with the predicted value 1.428 [point A in Fig. 2(c)]. The realization of 2D evanescent vortex beyond diffraction limit significantly boosts the information density and spatial pressure gradient, which is highly desirable for practical applications such as OAM-based communication and acoustic tweezer. For revealing the generality of our mechanism, we also use numerical simulations to demonstrate the capacity of our scheme to generate evanescent Bessel beams with other different orders. Figures 5(a)–5(c) show the simulated normalized amplitude and phase distributions of generated evanescent vortex with three particular topological charges $m = 0$, 2, and 4 in the x-y plane at $z = 1$ cm as well as 2D normalized amplitude distribution in the x-z plane, which exhibits the desired whole-area 2D Bessel patterns and near-field energy distributions for all three m. The slight energy leakages in z direction arise from the non-100% transmission and mode transformation efficiency of DLREs. Notice that for suppressing the spatial aliasing effect the number of elements and topological charge of generated vortex are

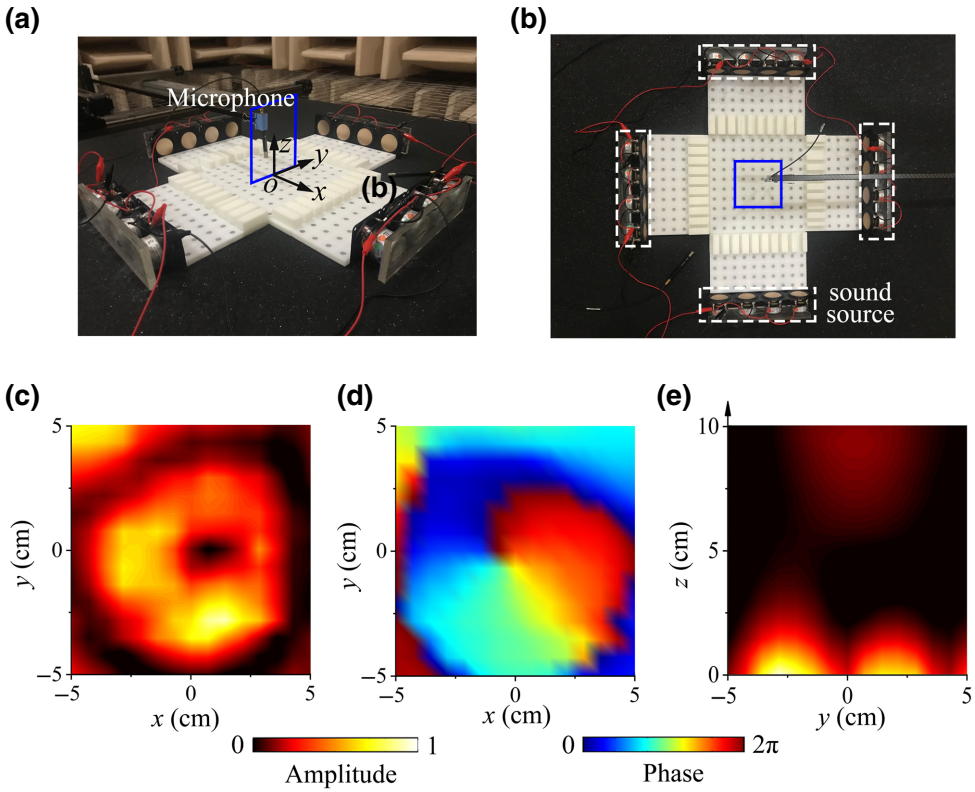

FIG. 6. Photographs of the 3D printed sample of designed surface and experimental setup from (a) front view and (b) top view. White dashed lines denote the line sources and origin $O(0,0,0)$ is located at the center of structured surface. (c) Measured sound amplitude and (d) phase distributions of 10×10 cm^2 square region in the x-y plane at $z = 1$ cm [marked by blue line in (b)]. (e) 2D measured sound amplitude distribution of 10×10 cm^2 square region in the vertical y-z plane at $x = 0$ cm [marked by the blue line in (a)]. The measurements are taken at every 2/3 cm in all three directions.

limited by condition $N > e\pi R_f/\lambda + m$ [12,14], where R_f and λ are the radius of the distortion-free vortex and acoustic wavelength in the background medium, respectively, calling for more unit cells for producing 2D vortex with higher orders.

V. EXPERIMENTAL MEASUREMENTS

The experimental measurement for generating first-order surface vortex is performed in an anechoic chamber, which can be regarded as an infinite free space for airborne sound. Figures 6(a) and 6(b) show the photos of the experimental setup and structured surface sample fabricated by 3D printing. We linearly assemble four 2-in. loudspeakers as the line source emitting a monochromatic plane wave of 3200 Hz. Four such line sources are synchronously driven by a multifunctional signal generator to guarantee the identical initial phase. The sound fields are measured by two 1/4-in. free-field microphones (Brüel & Kæjr type-4961) with one fixed as a reference signal while the other one is mounted on a 3D stepping motor to scan the target region point by point. By using the software PULSE Labshop, we obtain the cross spectrum of the two signals and thereby retrieve the sound phase and amplitude. We first measure 2D sound amplitude and phase distributions of a 10×10 cm^2 square region in the x-y plane at $z = 1$ cm [marked by blue line in Fig. 6(b)] and plot the experimental results in Figs. 6(c) and 6(d). The amplitude distribution in the vertical y-z plane at $x = 0$ cm [marked by blue line in Fig. 6(a)] is also scanned and the corresponding result is shown in Fig. 6(e). It can be clearly observed that the experimental results agree well with the simulation results with both showing null center, azimuthal dependence of phase, and exponential decay of intensity with z, validating the effectiveness of our mechanism for focusing 2D acoustic vortex beyond diffraction limit on the designed ultrathin structured surface. The slight distortion may stem from the imperfect fabrication and alignments of experimental sample. Although in the current study we demonstrate only a simple case of a square-shaped region surrounded by four line sources, it is apparent our proposed mechanism is general and has no dependence on the source type or the geometry of the target region, ensuring the application potential in more complicated practical environments.

VI. DISCUSSION

In conclusion, we propose to focus acoustic vortex beyond diffraction limit on an ultrathin structured surface by exciting and modulating the acoustic evanescent wave. As a practical implementation, we design a unit cell of DLRE to realize the arbitrary phase manipulation of evanescent wave in a subwavelength spatial scale. We theoretically derive the dispersion relationship of the supported evanescent wave and the desired azimuthal distribution of effective acoustical parameters needed for precise generation of evanescent vortex with target order. The performance of our mechanism is demonstrated via numerical simulation and experimental measurement by producing and focusing 2D vortices of desired order within a square region at subwavelength spatial resolution. Taking full advantage of the evanescent wave, our methodology with no need of a 2D system, bulky device size, geometric symmetry, active elements, or complicated phased array opens an avenue for the miniaturization and integration of planar vortex devices, with far-reaching implications in many diverse fields such as on-chip particle manipulation and information processing.

ACKNOWLEDGMENTS

This work is supported by National Key R&D Program of China (Grant No. 2017YFA0303700), the National Natural Science Foundation of China (Grants No. 11634006 and No. 81127901), a project funded by the Priority Academic Program Development of Jiangsu Higher Education Institutions, the Innovation Special Zone of National Defense Science and Technology and High-Performance Computing Center of Collaborative Innovation Center of Advanced Microstructures.

[1] L. Zhang and P. L. Marston, Geometrical interpretation of negative radiation forces of acoustical Bessel beams on spheres, Phys. Rev. E **84**, 035601 (2011).
[2] R. Lirette, J. Mobley, and L. Zhang, Ultrasonic Extraction and Manipulation of Droplets From a Liquid-Liquid Interface with Near-Field Acoustic Tweezers, Phys. Rev. Appl. **12**, 061001 (2019).
[3] J. Verbeeck, H. Tian, and P. Schattschneider, Production and application of electron vortex beams, Nature **467**, 301 (2010).
[4] M. Padgett and R. Bowman, Tweezers with a twist, Nat. Photonics **5**, 343 (2011).
[5] N. B. Simpson, K. Dholakia, L. Allen, and M. J. Padgett, Mechanical equivalence of spin and orbital angular momentum of light: An optical spanner, Opt. Lett. **22**, 52 (1997).
[6] X. Jiang, Y. Li, B. Liang, J. C. Cheng, and L. Zhang, Convert Acoustic Resonances to Orbital Angular Momentum, Phys. Rev. Lett. **117**, 034301 (2016).
[7] S. Mei, K. Huang, H. Liu, F. Qin, M. Q. Mehmood, Z. Xu, M. Hong, D. Zhang, J. Teng, A. Danner, and C. W. Qiu, On-chip discrimination of orbital angular momentum of light with plasmonic nanoslits, Nanoscale **8**, 2227 (2016).
[8] X. Jiang, C. Shi, Y. Wang, J. Smalley, J. Cheng, and X. Zhang, Nonresonant Metasurface for Fast Decoding in Acoustic Communications, Phys. Rev. Appl. **13**, 014014 (2020).
[9] Z. Tian, S. Yang, P. H. Huang, Z. Wang, P. Zhang, Y. Gu, H. Bachman, C. Chen, M. Wu, Y. Xie, and T. J. Huang, Wave

number–spiral acoustic tweezers for dynamic and reconfigurable manipulation of particles and cells, Sci. Adv. **5**, eaau6062 (2019).

[10] C. R. P. Courtney, C. E. M. Demore, H. Wu, A. Grinenko, P. D. Wilcox, S. Cochran, and B. W. Drinkwater, Independent trapping and manipulation of microparticles using dexterous acoustic tweezers, Appl. Phys. Lett. **104**, 154103 (2014).

[11] Z. Hong, J. Zhang, and B. W. Drinkwater, Observation of Orbital Angular Momentum Transfer From Bessel-Shaped Acoustic Vortices to Diphasic Liquid-Microparticle Mixtures, Phys. Rev. Lett. **114**, 214301 (2015).

[12] A. Grinenko, P. D. Wilcox, C. R. P. Courtney, and B. W. Drinkwater, Proof of principle study of ultrasonic particle manipulation by a circular array device, Proc. R. Soc. A **468**, 3571 (2012).

[13] Y. Chen, J. Gao, Z. Q. Jiao, K. Sun, W. G. Shen, L. F. Qiao, H. Tang, X. F. Lin, and X. M. Jin, Mapping Twisted Light Into and out of a Photonic Chip, Phys. Rev. Lett. **121**, 233602 (2018).

[14] J. J. Liu, B. Liang, J. Yang, J. Yang, and J. C. Cheng, Generation of non-aliased two-dimensional acoustic vortex with enclosed metasurface, Sci. Rep. **10**, 3827 (2020).

[15] J. Y. Lu, C. Y. Qiu, M. Z. Ke, and Z. Y. Liu, Valley Vortex States in Sonic Crystals, Phys. Rev. Lett. **116**, 093901 (2016).

[16] M. L. N. Chen, L. J. Jiang, and W. E. I. Sha, Generation of Orbital Angular Momentum by a Point Defect in Photonic Crystals, Phys. Rev. Appl. **10**, 014034 (2018).

[17] J. Shi, D. Ahmed, X. Mao, S. C. S. Lin, A. Lawit, and T. J. Huang, Acoustic tweezers: Patterning cells and microparticles using standing surface acoustic waves (SSAW), Lab Chip **9**, 2890 (2009).

[18] H. Z. Chen, T. Liu, H. Y. Luan, R. J. Liu, X. Y. Wang, X. F. Zhu, Y. B. Li, Z. M. Gu, S. J. Liang, H. Gao, L. Lu, L. Ge, S. Zhang, J. Zhu, and R. M. Ma, Revealing the missing dimension at an exceptional point, Nat. Phys. **16**, 571 (2020).

[19] W. Y. Tsai, Q. Sun, G. Hu, P. C. Wu, R. J. Lin, C. W. Qiu, K. Ueno, H. Misawa, and D. P. Tsai, Twisted surface plasmons with spin-controlled gold surfaces, Adv. Opt. Mater. **7**, 1801060 (2019).

[20] Y. Gorodetski, A. Niv, V. Kleiner, and E. Hasman, Observation of the Spin-Based Plasmonic Effect in Nanoscale Structures, Phys. Rev. Lett. **101**, 043903 (2008).

[21] G. Spektor, D. Kilbane, A. K. Mahro, B. Frank, S. Ristok, L. Gal, P. Kahl, D. Podbiel, S. Mathias, H. Giessen, F. J. Meyer Zu Heringdorf, M. Orenstein, and M. Aeschlimann, Revealing the subfemtosecond dynamics of orbital angular momentum in nanoplasmonic vortices, Science **355**, 1187 (2017).

[22] H. Kim, J. Park, S. W. Cho, S. Y. Lee, M. Kang, and B. Lee, Synthesis and dynamic switching of surface plasmon vortices with plasmonic vortex lens, Nano Lett. **10**, 529 (2010).

[23] T. Liu, F. Chen, S. Liang, H. Gao, and J. Zhu, Subwavelength Sound Focusing and Imaging via Gradient Metasurface-Enabled Spoof Surface Acoustic Wave Modulation, Phys. Rev. Appl. **11**, 034061 (2019).

[24] Y. Ye, M. Ke, Y. Li, T. Wang, and Z. Liu, Focusing of spoof surface-acoustic-waves by a gradient-index structure, J. Appl. Phys. **114**, 154504 (2013).

[25] N. Cselyuszka, M. Sečujski, N. Engheta, and V. Crnojević-Bengin, Temperature-controlled acoustic surface waves, New J. Phys. **18**, 103006 (2016).

[26] Y. Jin, B. Djafari-Rouhani, and D. Torrent, Gradient index phononic crystals and metamaterials, Nanophotonics **8**, 685 (2019).

[27] Y. Chen, H. Liu, M. Reilly, H. Bae, and M. Yu, Enhanced acoustic sensing through wave compression and pressure amplification in anisotropic metamaterials, Nat. Commun. **5**, 5247 (2014).

[28] X. Jiang, B. Liang, J. C. Cheng, and C. W. Qiu, Twisted acoustics: Metasurface-enabled multiplexing and demultiplexing, Adv. Mater. **30**, 1800257 (2018).

[29] C. Shi, M. Dubois, Y. Wang, X. Zhang, and P. Sheng, High-speed acoustic communication by multiplexing orbital angular momentum, Proc. Natl. Acad. Sci. U. S. A. **114**, 7250 (2017).

[30] L. Tong, Z. Xiong, Y. X. Shen, Y. G. Peng, X. Y. Huang, L. Ye, M. Tang, F. Y. Cai, H. R. Zheng, J. B. Xu, G. J. Cheng, and X. F. Zhu, An acoustic meta-skin insulator, Adv. Mater. **32**, 2002251 (2020).

[31] The physical properties of air at 293.15 K and standard atmospheric pressure are mass density $\rho_a = 1.21$ kg/m^3, sound speed $c_a = 343$ m/s, thermal conductivity $\kappa = 0.0258$ W/m K, dynamic viscosity $\mu = 1.81 \times 10^{-5}$ kg/m s, specific heat at constant pressure $C_p = 1.005 \times 10^3$ J/kg K, and ratio of specific heats $\gamma = 1.4$.

[32] L. Quan, F. Qian, X. Liu, X. Gong, and P. A. Johnson, Mimicking surface plasmons in acoustics at low frequency, Phys. Rev. B **92**, 104105 (2015).

[33] L. Quan, X. Zhong, X. Liu, X. Gong, and P. A. Johnson, Effective impedance boundary optimization and its contribution to dipole radiation and radiation pattern control, Nat. Commun. **5**, 3188 (2014).

[34] J. Zhu, J. Christensen, J. Jung, L. Martin-Moreno, X. Yin, L. Fok, X. Zhang, and F. J. Garcia-Vidal, A holey-structured metamaterial for acoustic deep-subwavelength imaging, Nat. Phys. **7**, 52 (2011).

[35] Y. Zhou, M. H. Lu, L. Feng, X. Ni, Y. F. Chen, Y. Y. Zhu, S. N. Zhu, and N. Ben Ming, Acoustic Surface Evanescent Wave and its Dominant Contribution to Extraordinary Acoustic Transmission and Collimation of Sound, Phys. Rev. Lett. **104**, 164301 (2010).

[36] T. Takahashi, K. Kuriyama, and T. Matsumoto, Beaming of inplane elastic waves through a subwavelength channel with periodic corrugations, Appl. Phys. Lett. **101**, 124101 (2012).